

Cite this: *Phys. Chem. Chem. Phys.*, 2011, **13**, 2242–2249

www.rsc.org/pccp

PAPER

## Interstitialcy diffusion of oxygen in tetragonal $\text{La}_2\text{CoO}_{4+\delta}$

Akihiro Kushima,<sup>a</sup> David Parfitt,<sup>b</sup> Alexander Chroneos,<sup>\*b</sup> Bilge Yildiz,<sup>\*a</sup>  
John A. Kilner<sup>b</sup> and Robin W. Grimes<sup>b</sup>

Received 25th August 2010, Accepted 3rd November 2010

DOI: 10.1039/c0cp01603a

We report on the mechanism and energy barrier for oxygen diffusion in tetragonal  $\text{La}_2\text{CoO}_{4+\delta}$ . The first principles-based calculations in the Density Functional Theory (DFT) formalism were performed to precisely describe the dominant migration paths for the interstitial oxygen atom in  $\text{La}_2\text{CoO}_{4+\delta}$ . Atomistic simulations using molecular dynamics (MD) were performed to quantify the temperature dependent collective diffusivity, and to enable a comparison of the diffusion barriers found from the force field-based simulations to those obtained from the first principles-based calculations. Both techniques consistently predict that oxygen migrates dominantly *via* an interstitialcy mechanism. The single interstitialcy migration path involves the removal of an apical lattice oxygen atom out from the LaO-plane and placing it into the nearest available interstitial site, whilst the original interstitial replaces the displaced apical oxygen on the LaO-plane. The facile migration of the interstitial oxygen in this path is enabled by the cooperative titling–untilting of the  $\text{CoO}_6$  octahedron. DFT calculations indicate that this process has an activation energy significantly lower than that of the direct interstitial site exchange mechanism. For 800–1000 K, the MD diffusivities are consistent with the available experimental data within one order of magnitude. The DFT- and the MD-predictions suggest that the diffusion barrier for the interstitialcy mechanism is within 0.31–0.80 eV. The identified migration path, activation energies and diffusivities, and the associated uncertainties are discussed in the context of the previous experimental and theoretical results from the related Ruddlesden–Popper structures.

### Introduction

Solid oxide fuel cells (SOFC) operating efficiently at the intermediate temperature range (500–700 °C)<sup>1</sup> are of technological importance. These temperatures, however, present difficulties for the electrochemical efficiency of traditional ceramic cathodes because of the high activation energies in their catalytic activity.<sup>2</sup> Among the perovskite-related materials, the Ruddlesden–Popper (RP) series of layered oxides (formula  $\text{A}_{n+1}\text{B}_n\text{O}_{3n+1}$ ) are considered to be promising for the next generation of intermediate temperature SOFCs (IT-SOFCs). RP phases were shown to possess appropriate electrochemical, electrical and catalytic properties combined with thermal and mechanical stability.<sup>3,4</sup> Additionally, the first members of the RP series with  $n = 1$ ,  $\text{A}_2\text{BO}_4$ , that exhibit the  $\text{K}_2\text{NiF}_4$  structure are also being considered for oxygen sensors and oxygen separation membranes.<sup>5–17</sup> These materials have been extensively investigated since the observation of high-temperature superconductivity in  $\text{La}_{2-x}\text{Ba}_x\text{CuO}_4$ .<sup>18</sup> An interesting and recent example of a

composite SOFC cathode has been the work of Sase *et al.*,<sup>19</sup> which demonstrated higher transport and an oxygen exchange rate that was higher by three orders of magnitude at the interface of the perovskite  $(\text{La,Sr})\text{CoO}_3$  and the RP phase  $(\text{La,Sr})_2\text{CoO}_4$ .

$\text{La}_2\text{NiO}_4$ , the first member of the RP family to be used as an SOFC cathode, was demonstrated to have fast oxygen transport over a wide temperature range, indicating that it is an important candidate cathode material.<sup>6,10</sup> For  $\text{La}_2\text{NiO}_4$ , previous experimental studies determined activation energies for oxygen diffusion in the range of 0.19 eV (for epitaxial thin films) to 0.90 eV (for single crystals).<sup>10,15,17</sup> Interestingly, a number of diffusion mechanisms were proposed for the oxygen transport in this material.<sup>6,10,15</sup> A summary of these results is given in Table 1. In this table the calculated activation energies are strictly the activation energies of the migration process. The most recent MD and experimental diffusion studies identified the oxygen interstitialcy mechanism of diffusion along the *ab* plane of the RP phase  $\text{La}_2\text{NiO}_4$  as being dominant, with an activation energy of around 0.5 eV.<sup>17,20</sup> Beyond the material structure considered here, the interstitialcy mechanism was found to govern the oxygen diffusion in broader classes of oxides, for example  $\text{MgO}$ .<sup>21,22</sup>

Substitution of the A- and/or B-site by other cations can further improve the electronic and ionic conductivity of

<sup>a</sup> Department of Nuclear Science and Engineering, Massachusetts Institute of Technology, 77 Massachusetts Avenue, Cambridge, MA 02139, USA. E-mail: byildiz@mit.edu

<sup>b</sup> Department of Materials, Imperial College London, London SW7 2AZ, UK. E-mail: alexander.chroneos@imperial.ac.uk

**Table 1** Activation energies of oxygen self-diffusion in  $A_2BO_{4+\delta}$ 

Material	$E_a$ /eV	Methodology	Comment	Reference
$La_2CoO_{4+\delta}$	0.12	Experimental		25
$La_2CoO_{4+\delta}$	1.27–1.39	DFT	Interstitial mechanism	Present study
$La_2CoO_{4+\delta}$	0.73–0.80	DFT	Interstitialcy mechanism	Present study
$La_2CoO_{4+\delta}$	0.31	MD	Interstitialcy mechanism	Present study
$Pr_2NiO_{4+\delta}$	0.49–0.64	MD	Interstitialcy mechanism	26
$La_2NiO_{4+\delta}$	0.51	MD	Interstitialcy mechanism	17
$La_2NiO_{4+\delta}$	1.2	DFT	Interstitial mechanism	11
$La_2NiO_{4+\delta}$	0.19	Experimental	Epitaxial thin film	15
$La_2NiO_{4+\delta}$	0.54	Experimental	Polycrystal, TOF-SIMS	20
$La_2NiO_{4+\delta}$	0.88	Experimental	Single crystal, $a$ - $b$ plane	10

$La_2NiO_4$  related structures.<sup>12,23</sup> Typically, La is substituted with Sr, and Ni with Co.<sup>12,24</sup> Isotopic exchange measurements of Co-doped  $La_2NiO_{4+\delta}$  determined a significant enhancement of the low-temperature (450–600 °C) ionic conductivity.<sup>25</sup> Atomistic simulations by Naumovich and Kharton<sup>23</sup> predicted that the substitution of  $Ni^{2+}$  with higher valence cations such as  $Fe^{3+}$  or  $Co^{3+}$  leads to increased oxygen interstitial concentration but is accompanied by a reduction in the diffusivity of the oxygen ions. Previous MD calculations in  $Pr_2NiO_{4+\delta}$  predicted that increases in the oxygen hyperstoichiometry can lead to a “stiffening” of the lattice and an increase of the migration energy barriers for oxygen interstitials.<sup>26</sup> While both the oxygen hyperstoichiometry and the higher valence B-site cations consistently imply a reduction in the oxygen diffusivity, the effect of both factors has yet to be systematically studied on the diffusion of oxygen in  $A_2BO_4$  materials. In the present study, using computational methods at two different scales, we assess a new model system, the tetragonal  $La_2CoO_{4+\delta}$ , where the Ni of  $La_2NiO_{4+\delta}$  is replaced with the higher valency Co. While there is a number of key theoretical reports on the bulk and surface structural nature of the  $LaCoO_3$  system,<sup>27,28</sup> to our knowledge this is the first report on the first principles-based and atomistic scale investigation for  $La_2CoO_{4+\delta}$ . Therefore, our investigation benefits from the cross-validation of the results between multiple simulation scales, and further comparison to the available experimental data is essential. We also compare the simulated oxygen migration paths, and the calculated energy barriers, and diffusivities in  $La_2CoO_{4+\delta}$  with previous results for  $La_2NiO_{4+\delta}$  and related materials.

## Computational methods

The computational approach integrates the use of DFT and MD calculations for a self-consistent validation of the results. The first principles-based calculations in the DFT formalism were performed to identify the precise mechanism and the energy barrier for the oxygen transport in  $La_2CoO_{4+\delta}$ . The atomistic simulations using MD were performed to quantify the diffusivity, and to enable a comparison of the diffusion barriers found from the force-field based simulations to those obtained from first-principles based calculations. Our calculated activation energies both from the DFT and from the MD simulations are strictly the activation energies of the migration process. The “effective diffusion barrier” depends both on the interstitial “migration” barrier and the interstitial “formation” energy in a coupled manner. The formation

energy and chemical potential drive the changes in the concentration of interstitials, effectively changing the diffusivity. Here, we fixed the oxygen stoichiometry in both the DFT and the MD calculations, and assessed only the migration barrier in both. Therefore, our calculations are self-consistent among each other in terms of the oxygen stoichiometry. For the dilute oxygen interstitial concentrations considered here, we assume that the interstitials do not interact considerably with each other, and thus, the calculated migration barrier closely represents the governing diffusion barrier. We expect that small deviations in  $\delta$  from the value considered here will not change the calculated activation energies significantly.

## Density functional theory calculations

Density functional theory formalism as implemented in the Vienna *Ab initio* Simulation Package (VASP)<sup>29,30</sup> was used to identify the ground state configurations and energies with and without the oxygen interstitial defects in the  $La_2CoO_4$  model. To avoid the self-interaction errors that occur in the traditional DFT for strongly correlated electronic systems, we employed the DFT + U method accounting for the on-site Coulomb interaction in the localized d or f orbitals.<sup>31,32</sup> An effective correction parameter, namely U-J, for the  $La_2CoO_4$  structure in DFT calculations is not found in literature. Therefore, we have selected a range of U-J correction parameters that are reported for the  $LaCoO_3$ , assuming similar electronic structures of Co in both the perovskite and the RP phases. This selected range of U-J parameters also allows us to assess the sensitivity of the diffusion barrier energies to the effective correction parameter value in the DFT calculations. A lower limit of U-J = 3.3 eV was chosen, as determined in ref. 33 and 34 by fitting the enthalpies of oxidation reactions. An upper limit of U-J = 5.85 eV was chosen, as determined in ref. 35 to represent an intermediate spin state of Co. The ionic cores were represented with the projector-augmented wave (PAW).<sup>36,37</sup> The exchange-correlation energy was evaluated by the generalized gradient approximation (GGA) using the Perdew–Burke–Ernzerhof (PBE) function.<sup>38</sup> An energy cut off of 400 eV was chosen for expanding the wave functions. The  $\Gamma$  point in the Brillouin zone was selected in the calculations. A  $2 \times 2 \times 1$  unit cell with 16 La, 8 Co, and 32 O atoms was used. 11 valence electrons for La ( $5s^25p^65d^1$ ), 9 for Co ( $3d^84s^1$ ) and 6 for O ( $2s^22p^4$ ) were considered as input in the energy-minimization calculations by VASP. The lattice parameters for the fully relaxed  $La_2CoO_4$  model were 3.89 Å ( $a,b$ ) and

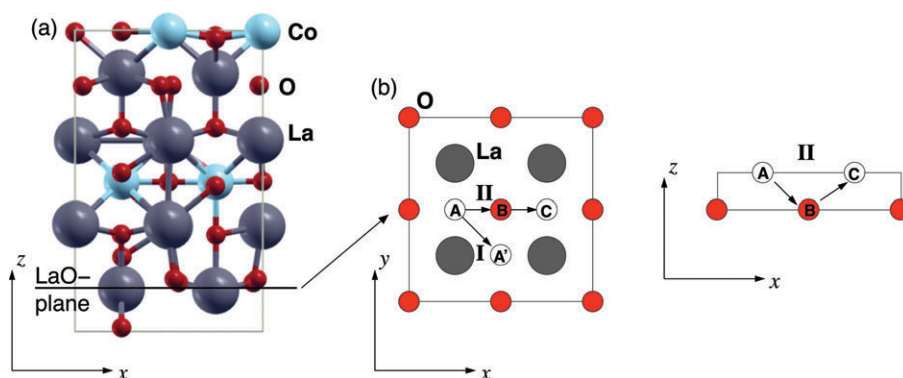


**Fig. 1** (a) Relaxed configuration of the  $\text{La}_2\text{CoO}_{4+\delta}$  model. Circled region shows the interstitial O atom. (b) Migration paths considered in the simulation: (I) O interstitial at site A directly hops to the adjacent interstitial site A'. This is the interstitial migration mechanism. (II) O interstitial at site A kicks the O atom at site B out from LaO plane placing it to the next interstitial site C, and placing itself to site B on the LaO plane. This is the interstitialcy migration mechanism. The white oxygen interstitial positions A, A' and C are out of the LaO-plane displayed by the grey La atoms and red O atoms.

12.4 Å (*c*), which agree with the experimentally measured values.<sup>12</sup> To introduce the oxygen interstitial, one oxygen atom was inserted into the position A in the  $\text{La}_2\text{O}_2$  layers of the relaxed  $\text{La}_2\text{CoO}_4$  cell configuration, as indicated in Fig. 1. The initial configuration for the interstitial oxygen migration was established by relaxing the atomic configuration, while fixing the cell parameters. We calculated the interstitial oxygen formation energy for this system to be  $-5.13$  eV; that is, very strongly favoring the uptake of oxygen interstitial. To find the minimum energy path, the configuration at the saddle point, and the energy barrier in the diffusion of the interstitial oxygen, we used the climbing image Nudged Elastic Band (NEB) method<sup>39</sup> as encoded in VASP. To identify the dominant diffusion mechanism for the interstitial oxygen, we assessed two possible migration pathways starting with this initial configuration, as schematically shown in Fig. 1: (I) the oxygen interstitial at site A directly hops to the adjacent interstitial site A'. (II) The O interstitial at site A kicks the O atom at site B out from the LaO plane, placing it to the next interstitial site C, while itself moving to site B on the LaO plane. These two pathways correspond to the so-called *interstitial* migration (path I) and *interstitialcy* migration (path II) mechanisms, respectively.

### Molecular dynamics simulations

In the MD framework Newton's equations of motion for an ensemble of particles are solved iteratively. These particles interact *via* potential energy functions, within the classical Born-like description of the ionic crystal lattice.<sup>40</sup> Ionic interactions are described by a long-range Coulombic potential (summed using Ewald's method)<sup>41</sup> and a short-range parameterized Buckingham pair potential.<sup>42</sup> The Buckingham pair potential is summed to the cut-off value of 10.5 Å, beyond

which the influence of the potential is considered negligible. The lattice energy is given by,

$$E_L = \sum_i \sum_{j>i} \left[ \frac{q_i q_j}{4\pi\epsilon_0 r_{ij}} + A_{ij} \exp\left(\frac{-r_{ij}}{\rho_{ij}}\right) - \left(\frac{C_{ij}}{r_{ij}^6}\right) \right] \quad (1)$$

where  $r_{ij}$  is the interionic separation between ions  $i$  and  $j$ ,  $q_i$  is the charge of ion  $i$ ,  $A_{ij}$ ,  $\rho_{ij}$  and  $C_{ij}$  are the short-range parameters of the Buckingham pair potential (see Table 2) and  $\epsilon_0$  is the permittivity of free space. The short-range parameters used here were reported in previous studies,<sup>7,43,44</sup> and their efficacy has been established for a number of complex oxide materials.<sup>45–50</sup>

Here we base the simulations on the high temperature tetragonal structure of  $\text{La}_2\text{CoO}_{4+\delta}$  determined by Skinner and Amow.<sup>12</sup> The periodic crystal lattice is constructed from a supercell of  $10 \times 10 \times 4$  unit cells consisting of around 5600 ions tessellated throughout space with the use of periodic boundary conditions as defined by the crystallographic lattice vectors.

For the integration of Newton's equations of motion we employed the velocity Verlet algorithm.<sup>51</sup> Ions were assigned a Gaussian distribution of velocities and with iterative velocity scaling, a stable temperature was obtained. The subsequent production runs that were used in the analysis were monitored after the system was equilibrated for 5000 time steps ( $\sim 5$  ps). For efficient sampling of the dynamic behaviour we used the variable time step option as incorporated in the DLPOLY code.<sup>52,53</sup> 250 000 time steps, with each time step of the order of 1 fs, were used to investigate oxygen diffusion in the temperature range 700–1500 K. The constant pressure (NPT) ensemble was applied to predict the equilibrium lattice parameters and the constant volume (NVT) ensemble to predict the diffusion properties with the volume of the cell set to the equilibrium value for the given temperature. Oxygen interstitial atoms were introduced randomly at the available interstitial sites within the cell. The extended equilibration period of 5000 time steps in the NPT ensemble and 5000 time steps in the NVT ensemble (total equilibration period of about  $\sim 10$  ps) is sufficient for the ions to reach quasi-equilibrium distributions. The Nosé–Hoover thermostat was used for corrections to the temperature and the pressure.<sup>54,55</sup>

**Table 2** Buckingham interionic potential parameters (see eqn (1))

Interaction	$A_{ij}/\text{eV}$	$\rho_{ij}/\text{\AA}$	$C_{ij}/\text{eV}\text{\AA}^6$	Reference
$\text{O}^{2-}-\text{O}^{2-}$	9547.96	0.2192	32.00	43
$\text{La}^{3+}-\text{O}^{2-}$	2119.79	0.3459	23.25	7
$\text{Co}^{3+}-\text{O}^{2-}$	1226.32	0.3087	0.00	44

Ionic diffusion is predicted by tracking the mean square displacement (MSD) of ions as a function of time for a range of temperatures. Adequate statistical sampling was ensured by implementing simulation times of 300 ps. At time  $t$  the MSD of an ion  $i$  at a position  $r_i(t)$  at time  $t$  with respect to its initial position  $r_i(0)$  is,

$$\langle r_i^2(t) \rangle = \frac{1}{N} \sum_{i=1}^N [r_i(t) - r_i(0)]^2 \quad (2)$$

where  $N$  is the total number of ions in the system.

The diffusion coefficient,  $D$ , is calculated directly from the slopes of MSD in a range of temperatures (here 800–1100 K) by using<sup>56</sup>

$$\langle |r_i(t) - r_i(0)|^2 \rangle = 6Dt + B \quad (3)$$

where  $|r_i(t) - r_i(0)|$  is the displacement of an oxygen ion from its initial position and  $B$  is an atomic displacement parameter attributed to thermal vibrations.

## Results and discussion

In this section, we first identify the dominant migration path by contrasting the energy barriers and charge distributions governing the interstitial and interstitialcy migration mechanisms for the oxygen, described as the paths I and II in Fig. 1. Then, the MD simulation results are introduced. We assess the collective nature of the oxygen diffusion represented by the temperature dependent MD simulations, and compare this to the first principles-based evaluation of the dominant diffusion paths.

### Oxygen migration mechanism and energy barriers

Fig. 2(a) shows the relative energy and the energy barriers  $E_B^I$  and  $E_B^{II}$  for oxygen diffusion *via* the interstitial and interstitialcy mechanisms, respectively, calculated using the NEB method. Reaction coordinates in Fig. 2(a) correspond to the paths described in Fig. 1 for both paths. The oxygen interstitial migration (path I) is associated with a 1.27–1.39 eV barrier, while the interstitialcy migration (path II) results in a 0.73–0.80 eV barrier, for the selected U-J values ranging from 3.3 to 5.85 eV. The relative ease of the indirect interstitialcy migration mechanism compared to the direct interstitial migration in the  $\text{La}_2\text{CoO}_{4+\delta}$  system is consistent with neutron diffraction<sup>14</sup> and MD<sup>17</sup> results probing the oxygen mass distribution in other  $\text{K}_2\text{NiF}_4$  type structures. Here, we explain the reason behind the relatively lower energy barrier of this migration path. First, we highlight the cooperative motion of the polyhedra surrounding the interstitial during its migration. The atomic structures along the interstitialcy migration (path II), at the initial (0), intermediate (1), and saddle (2) points are shown in Fig. 2(b). We note that the initial static structure of the  $\text{La}_2\text{CoO}_{4+\delta}$  consists of the  $\text{CoO}_6$  polyhedra that are tilted with their apical oxygen atoms away from the interstitial oxygen. This picture is consistent with the structural disorder identified in  $\text{La}_2\text{CoO}_{4+\delta}$  by neutron and X-ray diffraction.<sup>57</sup> To accommodate the interstitialcy migration, from the initial to the saddle state, the  $\text{CoO}_6$  octahedra cooperatively move from a tilted to an almost untilted

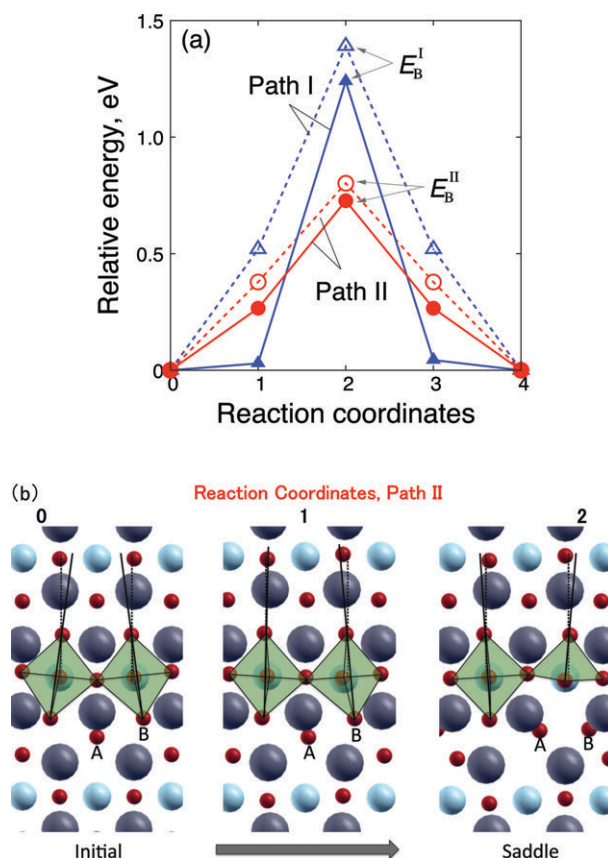


**Fig. 2** (a) The relative energy of the system along the oxygen diffusion paths *via* the interstitial and interstitialcy mechanisms, paths I and II in Fig. 1, respectively, calculated using the NEB method for the two selected U-J values. U-J = 5.85 eV for solid lines and filled symbols; U-J = 3.3 eV for dashed lines and open symbols. The calculated migration energy barriers,  $E_B^I$  and  $E_B^{II}$ , range as 1.27–1.39 eV and 0.73–0.80 eV for these U-J values. (b) Atomic structure along the interstitialcy migration (path II), at the initial, intermediate, and saddle points (reaction coordinates 0, 1, and 2 in (a)). A: interstitialcy oxygen atom, B: oxygen atom on the  $\text{LaO}$  plane. The  $\text{CoO}_6$  octahedra (shown in green) cooperatively moves from a tilted to an untilted configuration to accommodate the interstitialcy migration. The solid line in the figure connects the top and bottom oxygen atoms in the  $\text{CoO}_6$  octahedra, indicating the extent of tilt with respect to the reference dashed line drawn along  $z$  axis.

configuration. The tilt angle decreases as the structure evolves towards the saddle point. At the saddle point, the octahedra shows only a slight opposite tilt compared to that at the initial state. The result indicates that the cooperative lattice dynamics around the interstitial oxygen atom assists the interstitialcy migration, enabling a more facile transport path. Second, we turn our attention to the charge density distributions along each path that the oxygen passes through. The higher the charge density along the path, the more difficult it is for the oxygen to pass through. Fig. 3 shows the charge density distribution in the vicinity of the migrating oxygen, marked as A, at the initial and saddle points of the migration, displayed on the  $xy$  plane and the  $x = y$  plane for path I, and on the  $xz$  plane for path II. For path I, the direct interstitial migration, the oxygen A passes through a narrow



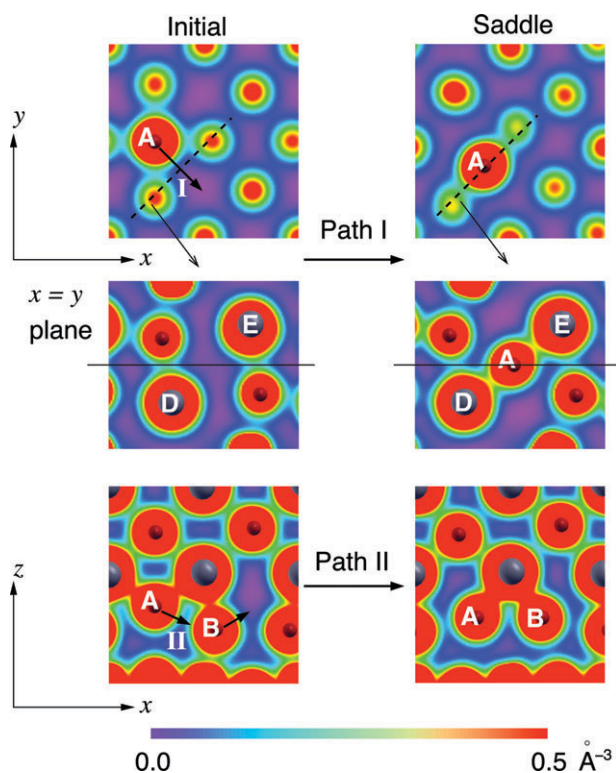


**Fig. 3** The charge density distribution in the vicinity of the migrating oxygen, marked as A, at the initial and saddle points of the migration paths, displayed on the  $xy$  plane and the  $x = y$  plane for path I (the interstitial), and the  $xz$  plane for path II (the interstitialcy). The middle panel for path I is on the  $x = y$  plane, indicated as the dashed line into the page on the upper panel of  $xy$  plane. The solid line on the  $x = y$  plane is the  $xy$  plane aligned with the migrating oxygen. Large gray spheres are La and small red spheres are O ions. The migrating interstitial oxygen is marked as A, the bridging La cations along path I are D and E, the lattice oxygen on the LaO plane is marked as B.

space between the two La cations, D and E, located just above and below the migration plane, forcing open the distance between these cations from 3.78 Å at the initial to 4.23 Å at the saddle configuration. Conversely, path II allows the oxygen A to go through a larger available opening with lower charge density, and this is enabled by the cooperative motion of the oxygen B as oxygen A approaches the lattice site B. Here, the atoms A and B “rotate” around the neighbouring La cation (as also implied in Fig. 2(b)), and the path does not involve the passing of either of the oxygen atoms through a narrow space with high density of electronic charge arising from the La cations. The relatively lower density of electronic charge without a narrow constriction by the La cations along the interstitialcy path and the lattice oxygen B leaving its site and moving towards an interstitial site at the saddle point renders this mechanism energetically more favourable. Lastly, we note that the diffusion barriers found from the DFT+U-NEB calculations are not very sensitive to the effective U-J parameter; a variation within 10% in the calculated barriers from U-J = 3.3 eV to 5.85 eV.

The charge state of the interstitial oxygen at its equilibrium initial and saddle states can affect the migration path and the barrier. We analyzed the Bader effective charge of the lattice

**Table 3** Bader effective charge of the apical lattice oxygen and the interstitial oxygen at the equilibrium and saddle points of migration paths I and II in  $\text{La}_2\text{CoO}_{4+\delta}$

	Path I (direct interstitial)	Path II (interstitialcy)
Lattice oxygen on the LaO plane at the initial equilibrium state	−1.34	−1.34
Lattice oxygen on the LaO plane at the saddle state	−1.33	−1.33
Interstitial oxygen at the initial equilibrium state	−1.26	−1.26
Interstitial oxygen at the saddle state	−1.23	−1.25

oxygen and the interstitial oxygen in the relaxed  $\text{La}_2\text{CoO}_{4+\delta}$  model. While a neutral oxygen atom (to maintain total neutrality of the model) is inserted as part of the model set up procedure, the DFT energy-minimization calculations relaxes the electrons to their equilibrium distribution at the ground state, and leaves behind a net charged interstitial oxygen. The resulting Bader effective charges of the interstitial oxygen in both path I and II are summarized in Table 3. The Bader charge of the apical lattice oxygen at the initial state is −1.34 and for the saddle point is −1.33, for both path I and II. For the interstitial oxygen, it is −1.26 at the initial equilibrium state, and −1.23 (path I) and −1.25 (path II) at saddle point. The interstitial oxygen is only slightly less charged than the apical oxygen whose formal charge is −2, as  $\text{O}^{2-}$ . However, the difference is not large enough to call the interstitial oxygen charge as −1. Therefore, we think that the interstitial oxygen in  $\text{La}_2\text{CoO}_{4+\delta}$  should also be formally (almost) −2, as  $\text{O}^{2-}$ . Furthermore, the charge is almost the same at the initial

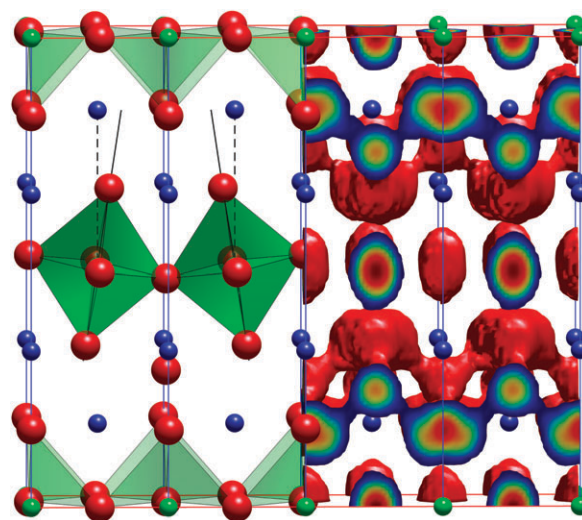


**Fig. 4** The isosurface connecting the oxygen conduction sites in  $\text{La}_2\text{CoO}_{4.125}$  from MD calculations at  $T = 1500$  K. The crystal structure of  $\text{La}_2\text{CoO}_{4+\delta}$  (O ions in red,  $\text{CoO}_6$  octahedra in green and La ions in blue) is also presented with the characteristic tilting of the  $\text{CoO}_6$  octahedra caused by the introduction of the oxygen interstitial.

equilibrium and the saddle points, and this suggests that no charge transfer takes place along the migration path. This result in  $\text{La}_2\text{CoO}_{4+\delta}$  is consistent with Frayret *et al.*'s<sup>11</sup> report for the charge state of the interstitial oxygen in  $\text{La}_2\text{NiO}_{4+\delta}$ .

### Temperature dependent collective oxygen diffusion

The present MD calculations support the DFT calculations in the assignment of the interstitial mechanism as the dominant mechanism for oxygen diffusion in  $\text{La}_2\text{CoO}_{4+\delta}$ . Fig. 4 is a predicted oxygen density profile of the interstitial mechanism of diffusion in the  $a$ - $b$  plane in  $\text{La}_2\text{CoO}_{4+\delta}$  at 1500 K. Essentially, the oxygen interstitial displaces an apical oxygen ion from the  $\text{CoO}_6$  octahedron on the LaO-plane, which then progresses to an adjacent oxygen interstitial site. We observe that the equatorial oxygen site also has a strongly anisotropic thermal ellipsoid. This is similar to the one observed experimentally by Skinner<sup>9</sup> and MD calculations<sup>17</sup> in  $\text{La}_2\text{NiO}_{4+\delta}$ , MD calculations in  $\text{Pr}_2\text{NiO}_{4+\delta}$ ,<sup>26</sup> and the maximum entropy method results of Yashima *et al.*<sup>14</sup> for related oxides. The oxygen density of the apical oxygen is consistent with the DFT findings of octahedral tilting during the migration of the interstitial, shown on the LHS of Fig. 2 and 4.

Within the temperature range considered here, 700–1500 K, the lanthanum and cobalt cations oscillate around their equilibrium positions, whereas oxygen ions demonstrate an increased MSD with time. This is consistent with previous studies in perovskite-related oxides, in which it was determined that cation diffusion coefficients are orders of magnitude lower than oxygen diffusion coefficients.<sup>58</sup>

Fig. 5 is an Arrhenius plot of the calculated oxygen diffusivities of  $\text{La}_2\text{CoO}_{4.12}$  as compared with previous

experimental results.<sup>25</sup> We used two MD approaches to calculate the diffusivities. In the first approach the unit cell parameters were calculated using an NPT equilibration before the production runs in the NVT ensemble (inverse triangles in Fig. 5). In the first approach we found an activation energy for oxygen diffusion of 0.31 eV effectively within 0.2 eV of the experimental value (0.12 eV, ref. 25), however, the calculated diffusivities (inverse triangles in Fig. 5) are significantly lower compared to the experimentally determined values of Munnings *et al.*<sup>25</sup> (black triangles in Fig. 5). In this approach to facilitate the oxygen transport and correlated octahedral movement,

the cells expanded especially at high temperatures, where the oxygen diffusion is more pronounced. In experiment  $\text{La}_2\text{CoO}_{4+\delta}$  is not stable in air above  $\sim 950$  K as noted by Munnings *et al.*,<sup>25</sup> however, in the MD calculations the interatomic potentials rendered the tetragonal structure stable, even at 1500 K, although the structure might be approaching instability with weaker bonds in the MD simulations. Given the close correspondence of the energy barrier results of these interatomic potential models with the experimental studies regarding related compounds (Fig. 5, Table 1 and references therein, see below), our results suggest that oxygen transport in  $\text{La}_2\text{CoO}_{4+\delta}$  is significant as it is in most other materials with the  $\text{K}_2\text{NiF}_4$  structure. The second approach corresponds to calculations in the NVT ensemble, where the unit cell parameters were equal to the ones predicted by DFT. These results effectively represent the situation where  $\text{La}_2\text{CoO}_{4+\delta}$  is constrained at a constant volume independent of the temperature. In Fig. 5 these NVT-predicted diffusivities (white triangles) are at the same order of magnitude and slightly underestimate the experimental results of Munnings *et al.*<sup>25</sup> (black triangles in Fig. 5) and the previous MD<sup>17</sup> and experimental<sup>20</sup> results for  $\text{La}_2\text{NiO}_{4+\delta}$ . Interestingly, in this second approach the activation energy for oxygen diffusion is calculated to be 0.23 eV and is effectively equivalent to the experimental value (0.12 eV, ref. 25).

### Comparison with experiment and related materials

Here, we discuss our results in the context of prior measurements and simulations, and consider the consistencies and the uncertainties in the experimental reports on  $\text{La}_2\text{CoO}_{4+\delta}$  as well as in our simulation methods. We have previously shown that the MD calculations are in excellent agreement with experiments in the case of  $\text{La}_2\text{NiO}_{4+\delta}$ .<sup>17,20</sup> In Fig. 5 we compare the MD predictions of diffusivity to the experimental results for  $\text{La}_2\text{CoO}_{4+\delta}$  and  $\text{La}_2\text{NiO}_{4+\delta}$ . For  $\text{La}_2\text{NiO}_{4+\delta}$  the calculated diffusivities are of the same order of magnitude with respect to the experimental data of Sayers *et al.*<sup>20</sup> (Fig. 5). Additionally, the calculated activation energy for oxygen diffusion in  $\text{La}_2\text{NiO}_{4+\delta}$  (0.51 eV, ref. 17) is in excellent agreement with the determined activation energy (0.54 eV, ref. 20). In Fig. 5 we compare with the study of Sayers *et al.*<sup>20</sup> not only because it is the most recent experimental work on  $\text{La}_2\text{NiO}_{4+\delta}$  but also because it is the most advanced diffusion study on  $\text{La}_2\text{NiO}_{4+\delta}$  with the concentration-depth profiles being determined by both an Atomika SIMS instrument and the state of the art ToF-SIMS instrument.<sup>20</sup> Notably,

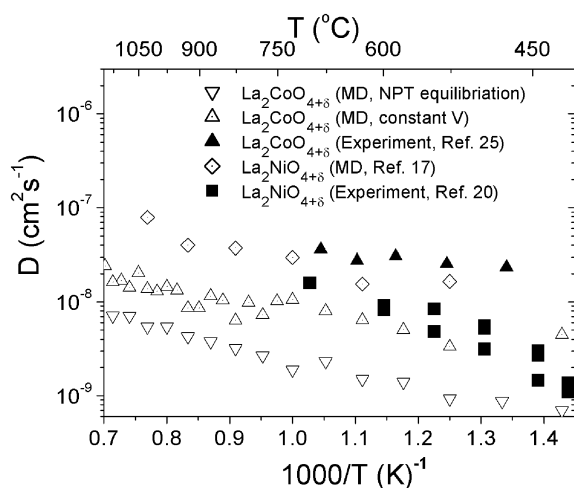


**Fig. 5** Arrhenius plot of the calculated oxygen diffusivity in the  $a$ - $b$  plane of  $\text{La}_2\text{CoO}_{4+\delta}$  as compared to previous experimental evidence for  $\text{La}_2\text{CoO}_{4+\delta}$  (ref. 25). For comparison the MD and experimental results for  $\text{La}_2\text{NiO}_{4+\delta}$ .<sup>17,20</sup> are also presented. The inverse triangles correspond to MD calculations for  $\text{La}_2\text{CoO}_{4+\delta}$  where the unit cell parameters were calculated using an NPT equilibration before the production runs in the NVT ensemble. The white triangles correspond to NVT ensemble calculations where the unit cell parameters were equal to the ones predicted by DFT. The  $\delta$  value for all the MD calculation is approximately 0.12.

however, as discussed previously the calculated diffusivities are also consistent with most previous experimental studies on  $\text{La}_2\text{NiO}_{4+\delta}$  (ref. 17 and references therein).

To facilitate further comparison of our results on  $\text{La}_2\text{CoO}_{4+\delta}$  with related materials, we report in Table 1 the activation energies of oxygen self-diffusion in  $\text{A}_2\text{BO}_{4+\delta}$ . The predicted (MD and DFT) interstitialcy mechanism for diffusion in the  $a$ - $b$  plane of  $\text{La}_2\text{CoO}_{4+\delta}$  is analogous to the MD derived mechanism for  $\text{La}_2\text{NiO}_{4+\delta}$  and  $\text{Pr}_2\text{NiO}_{4+\delta}$ .<sup>17,26</sup> The activation energy of  $\text{La}_2\text{CoO}_{4+\delta}$  calculated by MD, is in reasonable agreement with experiment but significantly lower compared to the present DFT calculations. Regarding the interstitial mechanism (path I) the activation energy of 1.27–1.39 eV calculated here for  $\text{La}_2\text{CoO}_{4+\delta}$  is essentially identical to the activation energy of 1.2 eV predicted by Frayret *et al.*<sup>11</sup> using DFT for  $\text{La}_2\text{NiO}_{4+\delta}$  (see Table 1).

In the experimental results for  $\text{La}_2\text{CoO}_{4+\delta}$  the possible role of extended defects, such as dislocations and grain boundaries, as faster transport pathways is unclear, however the diffusion data reported in the literature<sup>25</sup> is consistent with bulk oxygen diffusion. One of the main problems with the experimental data is that, as noted by the authors, the stoichiometry of the materials is changing with temperature and that this could lead to an erroneous assignment of the migration enthalpy, rendering the measured 0.12 eV debatable. Even the migration mechanism details may change with stoichiometry due to possible interactions among the interstitial defects, for example the interstitial ordering as reported by Le Toquin *et al.*<sup>57</sup> This experimental uncertainty related to the temperature dependent stoichiometry is true of many of the measurements of these perovskite and perovskite related materials however this could be particularly exacerbated by the relative instability of this material at high temperatures and high oxygen pressures. As noted before, here we fixed the oxygen stoichiometry in both the DFT and the MD calculations, and assessed only the migration barrier in both. Therefore, our calculations are self-consistent among each other in terms of the oxygen stoichiometry. Our results do not explicitly take into account the temperature dependent changes in oxygen interstitial fraction which would alter the diffusivity and the effective diffusion barrier. However, for the dilute interstitial fraction considered here, we expect that the calculated migration barrier closely represents the governing diffusion barrier.

In addition to the uncertainties in the experimental reports, there are a number of important simulation details which add to the uncertainties in our quantitative estimates. The simple interatomic interactions used in the MD calculations cannot simulate the Co spin, and the accurate electronic state explicitly. Furthermore, the MD simulation temperatures above the experimental stability temperature range of the  $\text{La}_2\text{CoO}_{4+\delta}$  might lead to a relatively lower activation barrier (0.31 eV) than the true barrier at the given stoichiometry. The Co spin state representation is possible and important, on the other hand nontrivial in the DFT. While there are several reports regarding this for  $\text{LaCoO}_3$ , there is scarce information for  $\text{La}_2\text{CoO}_4$ . The U-correction term taking into consideration the self-interaction errors can sensitively influence the spin state of the Co and the resulting energetics. In the present study we adopted the U-J effective correction term from

published results on  $\text{LaCoO}_3$ , however, the DFT-calculated barriers were within 10% of each other within a relative large range of U-J from 3.3 eV to 5.85 eV, rendering the results less sensitive to this parameter. Probably, the most important uncertainty in the DFT calculations is the size of the simulation cell. Due to the computational expense of the problem, we worked with a relatively small unit cell size of  $2 \times 2 \times 1$ , with 56 lattice atoms, and 1 interstitial oxygen atom. Although the NEB seeks to trace the minimum energy migration energy path, the relative relaxation of the unit cell, and the interaction between the interstitial defects in image cells depend on the unit cell size. Even though the tilt distortion of the  $\text{CoO}_6$  octahedra at the initial state is adequately accounted for in the DFT structure (Fig. 2(b) LHS vs. Fig. 4, LHS), the smaller the unit cell size, the more constrained the relaxation is during the migration in the NEB runs, and thus, this DFT cell size may lead to a relatively larger diffusion barrier (0.73–0.80 eV) compared to its true value at the chosen stoichiometry. Lastly, the charge state of the interstitial oxygen in the MD and DFT treatments could have led to a discrepancy. However, there is a consistency between the MD input charge and the DFT estimated charge, given that the Bader charge calculations (Table 1) suggest 2– for the interstitial oxygen's charge. Therefore, the difference in the charge state of the interstitial oxygen cannot be the reason for the difference in the MD- and DFT-predicted migration energies.

Finally, while we consider the uncertainties in the experiments and in the simulations as discussed above, we believe that they do not affect the mechanistic results that we found consistently from the MD and DFT calculations, but rather affect the quantitative results. In light of these observations, we conclude that the oxygen diffusion in  $\text{La}_2\text{CoO}_{4+\delta}$  is certainly governed by the interstitialcy mechanism, and is associated with an energy barrier between 0.31 eV to 0.80 eV.

## Conclusions

In the present study we used DFT and MD techniques to predict the mechanism and energetics of oxygen transport in tetragonal  $\text{La}_2\text{CoO}_{4+\delta}$ . Importantly, both techniques are consistent in identifying the interstitialcy mechanism of oxygen diffusion. This involves the cooperative motion of the  $\text{CoO}_6$  octahedra surrounding the oxygen interstitial along its migration, enabling a facile interstitialcy transport path. However, the predicted activation energies by DFT and MD differ from each other, and this can be attributed to the different structural and electronic assumptions applied. Our results can motivate additional diffusion experiments on single crystal structures with well-controlled stoichiometries to further clarify the energetics of oxygen transport in  $\text{La}_2\text{CoO}_{4+\delta}$  as a potentially important fast oxygen conductor at reduced temperatures.

## Acknowledgements

The authors thank Dr Stephen Skinner (Imperial College London) for useful discussions. BY and AK acknowledge the US-DOE-Basic Energy Sciences, Grant No.DE-SC0002633 for financial support, and the National Science Foundation for



computational support through the TeraGrid Advanced Support Program, Grant No. TG-ASC090058. AC and JAK acknowledge support from the EPSRC SOFC platform grant EP/F009720/1 “New Research Directions for Solid Oxide Fuel Cell Science and Engineering”. Computing resources were partially provided by the HPC facility of Imperial College London.

## References

- N. P. Brandon, S. Skinner and B. C. H. Steele, *Annu. Rev. Mater. Res.*, 2003, **33**, 183.
- J. Fleig, *Annu. Rev. Mater. Res.*, 2003, **33**, 361.
- V. V. Kharton, A. P. Viskap, E. N. Naumovich and F. M. B. Marques, *J. Mater. Chem.*, 1999, **9**, 2623.
- A. Tarancón, M. Burriel, J. Santiso, S. J. Skinner and J. A. Kilner, *J. Mater. Chem.*, 2010, **20**, 3799.
- V. V. Vashook, N. E. Trofimenko, H. Ullmann and L. V. Makhnach, *Solid State Ionics*, 2000, **131**, 329.
- S. J. Skinner and J. A. Kilner, *Solid State Ionics*, 2000, **135**, 709.
- L. Minervini, R. W. Grimes, J. A. Kilner and K. E. Sickafus, *J. Mater. Chem.*, 2000, **10**, 2349.
- F. Mauvy, J. M. Bassat, E. Boehm, J. P. Manaud, P. Dordor and J. C. Grenier, *Solid State Ionics*, 2003, **158**, 17.
- S. J. Skinner, *Solid State Sci.*, 2003, **5**, 419.
- J. M. Bassat, P. Odierb, A. Villesuzanne, C. Marinc and M. Pouchard, *Solid State Ionics*, 2004, **167**, 341.
- C. Frayret, A. Villesuzanne and M. Pouchard, *Chem. Mater.*, 2005, **17**, 6538.
- S. J. Skinner and G. Amow, *J. Solid State Chem.*, 2007, **180**, 1977.
- A. R. Cleave, J. A. Kilner, S. J. Skinner, S. T. Murphy and R. W. Grimes, *Solid State Ionics*, 2008, **179**, 823.
- M. Yashima, M. Enoki, T. Wakita, R. Ali, Y. Matsushita, F. Izumi and T. Ishihara, *J. Am. Chem. Soc.*, 2008, **130**, 2762.
- M. Burriel, G. Garcia, J. Santiso, J. A. Kilner, R. J. Chater and S. J. Skinner, *J. Mater. Chem.*, 2008, **18**, 416.
- D. Rupasov, A. Chroneos, D. Parfitt, J. A. Kilner, R. W. Grimes, S. Ya. Istomin and E. V. Antipov, *Phys. Rev. B: Condens. Matter Mater. Phys.*, 2009, **79**, 172102.
- A. Chroneos, D. Parfitt, J. A. Kilner and R. W. Grimes, *J. Mater. Chem.*, 2010, **20**, 266.
- J. G. Bednorz and K. A. Müller, *Z. Phys. B: Condens. Matter*, 1986, **64**, 189.
- M. Sase, K. Yashiro, K. Sato, J. Mizusaki, T. Kawada, N. Sakai, K. Yamaji, T. Horita and H. Yokokawa, *Solid State Ionics*, 2008, **178**, 1843.
- R. Sayers, R. A. De Souza, J. A. Kilner and S. J. Skinner, *Solid State Ionics*, 2010, **181**, 386.
- T. Brudevoll, E. A. Kotomin and N. E. Christensen, *Phys. Rev. B: Condens. Matter*, 1996, **53**, 7731.
- E. A. Kotomin and A. Popov, *Nucl. Instrum. Methods Phys. Res., Sect. B*, 1998, **141**, 1.
- E. N. Naumovich and V. V. Kharton, *THEOCHEM*, 2010, **946**, 57.
- J. A. Kilner and C. K. M. Shaw, *Solid State Ionics*, 2002, **154–155**, 523.
- C. N. Munnings, S. J. Skinner, G. Amow, P. S. Whitfield and I. J. Davidson, *Solid State Ionics*, 2005, **176**, 1895.
- D. Parfitt, A. Chroneos, J. A. Kilner and R. W. Grimes, *Phys. Chem. Chem. Phys.*, 2010, **12**, 6834.
- M. S. D. Read, M. S. Islam, G. W. Watson, F. King and F. E. Hancock, *J. Mater. Chem.*, 2000, **10**, 2298.
- Y. Lee, J. Kleis, J. Rossmeisl and D. Morgan, *Phys. Rev. B: Condens. Matter Mater. Phys.*, 2009, **80**, 224101.
- G. Kresse and J. Hafner, *Phys. Rev. B: Condens. Matter*, 1993, **47**, 558.
- G. Kresse and J. Furthmüller, *Phys. Rev. B: Condens. Matter*, 1996, **54**, 11169.
- V. I. Anisimov, J. Zaanen and O. K. Andersen, *Phys. Rev. B: Condens. Matter*, 1991, **44**, 943.
- V. I. Anisimov, F. Aryasetiawan and A. I. Lichtenstein, *J. Phys.: Condens. Matter*, 1997, **9**, 767.
- L. Wang, T. Maxisch and G. Ceder, *Phys. Rev. B: Condens. Matter Mater. Phys.*, 2006, **73**, 195107.
- Y. Lee, J. Kleis, J. Rossmeisl and D. Morgan, *Phys. Rev. B: Condens. Matter Mater. Phys.*, 2009, **80**, 224101.
- Z. Yang, Z. Huang, L. Ye and X. Xie, *Phys. Rev. B: Condens. Matter Mater. Phys.*, 1999, **60**, 15674.
- G. Kresse and D. Joubert, *Phys. Rev. B: Condens. Matter Mater. Phys.*, 1998, **59**, 1758.
- P. E. Blöchl, *Phys. Rev. B: Condens. Matter*, 1994, **50**, 17953.
- J. Perdew, K. Burke and M. Ernzerhof, *Phys. Rev. Lett.*, 1996, **77**, 3865.
- G. Henkelman, B. P. Uberuaga and H. Jónsson, *J. Chem. Phys.*, 2000, **113**, 9901.
- M. Born and J. E. Mayer, *Z. Phys.*, 1932, **75**, 1.
- P. P. Ewald, *Ann. Phys. (Leipzig)*, 1921, **64**, 253.
- R. A. Buckingham, *Proc. R. Soc. London, Ser. A*, 1938, **168**, 264.
- R. W. Grimes, D. J. Binks and A. B. Lidiard, *Philos. Mag. A*, 1995, **72**, 651.
- D. J. Binks, *PhD thesis*, University of Surrey, 1994.
- R. W. Grimes, G. Busker, M. A. McCoy, A. Chroneos, J. A. Kilner and S. P. Chen, *Ber. Bunsen-Ges. Phys. Chem.*, 1997, **101**, 1204.
- R. A. De Souza and J. Maier, *Phys. Chem. Chem. Phys.*, 2003, **5**, 740.
- G. Busker, A. Chroneos, R. W. Grimes and I. W. Chen, *J. Am. Ceram. Soc.*, 1999, **82**, 1553.
- M. R. Levy, C. R. Stanek, A. Chroneos and R. W. Grimes, *Solid State Sci.*, 2007, **9**, 588.
- A. Chroneos, N. Ashley, K. Desai, J. F. Maguire and R. W. Grimes, *J. Mater. Sci.*, 2007, **42**, 2024.
- A. Chroneos, R. V. Vovk, I. L. Goulatis and L. I. Goulatis, *J. Alloys Compd.*, 2010, **494**, 190.
- W. C. Swope, H. C. Andersen, P. H. Berens and K. R. Wilson, *J. Chem. Phys.*, 1982, **76**, 637.
- W. Smith and T. R. Forester, *J. Mol. Graphics*, 1996, **14**, 136.
- W. Smith and I. Todorov, *The DLPOLY 3.0 User Manual*, Daresbury Laboratory, UK.
- S. Nosé, *J. Chem. Phys.*, 1984, **81**, 511.
- W. G. Hoover, *Phys. Rev. A: At., Mol., Opt. Phys.*, 1985, **31**, 1695.
- M. J. Gillan, *Physica B+C*, 1985, **131**, 157.
- R. Le Toquin, W. Paulus, A. Cousson, G. Dhalenne and A. Revcolevschi, *Physica B+C*, 2004, **350**, e269.
- S. Miyoshi and M. Martin, *Phys. Chem. Chem. Phys.*, 2009, **11**, 3063.